AGU PUBLICATIONS

Geophysical Research Letters

RESEARCH LETTER
10.1002/2015GL066917

Key Points:
- The moment magnitude of this earthquake is 3.9 and its mechanism is dominated by strike slip
- Full moment tensor inversions can recover the hypocenter location and depth to an accuracy of 1 km
- The focal depth of 3 to 4 km is within the Duvernay formation, close to the crystalline basement

Supporting Information:
- Table S1 and Figures S1 and S2
- Figure S1
- Figure S2

Correspondence to:
R. Wang,
ruijia3@ualberta.ca

Citation:
Wang, R., Y. J. Gu, R. Schultz, A. Kim, and G. Atkinson (2016), Source analysis of a potential hydraulic-fracturing-induced earthquake near Fox Creek, Alberta, *Geophys. Res. Lett.*, *43*, 564–573, doi:10.1002/2015GL066917.

Received 6 NOV 2015
Accepted 15 DEC 2015
Accepted article online 17 DEC 2015
Published online 19 JAN 2016
Corrected 5 FEB 2016

This article was corrected on 5 FEB 2016. See the end of the full text for details.

Source analysis of a potential hydraulic-fracturing-induced earthquake near Fox Creek, Alberta

Ruijia Wang[1], Yu Jeffrey Gu[1], Ryan Schultz[2], Ahyi Kim[3], and Gail Atkinson[4]

[1]Department of Physics, University of Alberta, Edmonton, Alberta, Canada, [2]Alberta Geological Survey, Edmonton, Alberta, Canada, [3]Department of Materials System Science, Yokohama City University, Yokohama City, Japan, [4]Department of Earth Sciences, University of Western Ontario, London, Ontario, Canada

Abstract An earthquake with a reported magnitude of 4.4 (M_L) was detected on 13 June 2015 in western central Alberta, Canada. This event was the third felt earthquake this year near Fox Creek, a shale gas exploration region. Our results from full moment tensor inversions of regional broadband data show a strong strike-slip mechanism with near-vertical fault plane solutions. The decomposition of the moment tensor solution is overwhelmingly double couple, while only a modest (~20%) contribution is attributed to compensated-linear-vector-dipole. The depth of this earthquake is 3–4 km, near the base of the sedimentary layer, and the moment magnitude (**M** = 3.9) of this event is considerably smaller than the initial reported M_L value. The hypocenter location, depth, and mechanism are favorable to a possible association between this earthquake and hydraulic fracturing operations within the Duvernay shale.

1. Introduction

On 13 June 2015, an earthquake with a reported magnitude (M_L) of 4.4 occurred roughly 30 km south of Fox Creek, Alberta, Canada. This was the third moderate earthquake in this historically quiescent region in less than 6 months; no $M_L > 3.5$ events have been recorded within 100 km of the hypocenter prior to 2015 (NRC Earthquake Database, http://earthquakescanada.nrcan.gc.ca/stndon/NEDB-BNDS/bull-eng.php). All three events have been suspected to be associated with hydraulic fracturing (HF) operations, which were responsible for the 2013–2014 Crooked Lake earthquake swarm 30 km west of Fox Creek [*Schultz et al.*, 2015a]. The June 2015 earthquake is significant for both political and scientific reasons. It was potentially the largest HF-induced earthquake in the world and was the first earthquake that triggered the stop light for HF operations in compliance with a newly enacted "traffic light" regulation in Canada [*Alberta Energy Regulator*, 2015].

The hypocenter of this earthquake resides within the Chinchaga domain, an early Proterozoic plutonic/metamorphic terrane roughly 30 km from a splay of the Snowbird Tectonic Zone [*Gu and Shen*, 2015; *Jones*, 2002] near basement depth [*Pilkington et al.*, 2000]. The sedimentary strata above the basement rocks are highlighted by the Duvernay Formation, which originated as a fill-in basin coeval with the Leduc reef [*Rokosh et al.*, 2010; *Switzer et al.*, 1994]. Both conventional and unconventional hydrocarbon exploration activities are presently taking place in the Duvernay play, many assisted by HF, the suspected source of recent earthquakes in this region.

However, questions have surfaced in the past few months regarding the reported magnitudes, which differ by 0.6 magnitude units among five different reporting agencies; hypocenter locations vary by as much as 26 km. Much of the discrepancy may be attributed to (1) limited seismic station density and/or incomplete use of available data; (2) uneven station coverage, especially along the NE-SW orientation; (3) phase picking inaccuracies associated with automatic solutions; and (4) the lack of consideration for an appropriately calibrated attenuation model of the Western Canada Sedimentary Basin (WCSB). Disagreements among the existing source solutions underscore the challenges in the assessment of the nature of this event, which is crucial for regional seismic monitoring, regulatory practices, and hazard mitigation [*Bent*, 2011].

This study presents an updated analysis of the earthquake source parameters from full moment tensor inversions of broadband recordings and a discussion of regional ground motion observations. The availability of local data, particularly recordings from two recently installed stations, and a grid search algorithm enable

us to determine the hypocenter location and depth to an accuracy of ~1 km. This event (**M**=3.9) is located within the Duvernay play at a depth close to the basement and exhibits a strike-slip mechanism. The significance of these findings will be discussed in relation to the regional geology and HF operations.

2. Data and Methods

The waveforms analyzed in this study are broadband recordings from TransAlta (TD), Regional Alberta Seismic Observatory for Earthquake Studies Network (RAVEN) [*Schultz and Stern*, 2015], and Canadian Rockies and Alberta Network (CRANE) [*Gu et al.*, 2011] (Figure 1). The stations are uniformly distributed around the source area, with distances ranging from 30 to 300 km. Other recordings that are publicly available in real time from all networks are also utilized to compare ground motion amplitudes to regional attenuation models. After deconvolving the instrument responses, we rotate the three-component seismograms to the great circle and then filter the waveforms based on frequency ranges of 0.08–0.4 Hz and 0.05–0.1 Hz to enable simultaneous inversions of both body and surface wave waveforms. Various source parameters are then retrieved from full and deviatoric moment tensor inversions and verified against solutions from an independent forward modeling procedure with the constraint of the pure double couple (DC) [*Henry et al.*, 2002]. Six moment tensor elements are determined through the full moment tensor inversion, whereas the deviatoric solution assumes no net volume change (i.e., isotropic component = 0) [*Julian et al.*, 1998] and recovers five independent tensor elements. Our inversion method is based on the tdmt-invc-iso package [*Minson and Dreger*, 2008; *Dreger*, 2003] and the Green's functions are computed from frequency wave number integrations [*Saikia*, 1994]. This study extends the original package to enable a flexible, simultaneous inversion of multiple frequencies and phases [*Chen et al.*, 2015a]. Moreover, pure DC moment tensors are generated from forward modeling of possible strike, dip, and rake angles with a step size of 5°.

Independent solutions of full, deviatoric, and pure DC are obtained using an assumed focal depth of 5 km, an effective average of the reported values from five different agencies (SLU, AGS, NRC, NMX, and NEIC). For the Green's function calculations we assume a one-dimensional velocity structure that combines the upper crust model from *Welford and Clowes* [2006] with a middle crust/upper mantle model from *Chen et al.* [2015b]. A modified model [*Zelt and Ellis*, 1990] which was determined from seismic refraction data sampling the Peace River Arch region, is adopted to characterize the attenuation structure of the study area down to 100 km depth.

Two weighting schemes are explored during the inversion and forward modeling based on the considerations of (1) the amplitude ratio between body and surface waves and (2) the reciprocal of source-station distances. Time shifts are introduced during the fitting procedure to minimize the effects of velocity heterogeneity and earthquake mislocation [*Dreger*, 2003]. The quality of waveform matching is assessed through the variance reduction (VR) and normalized residual (RES/Pdc) [*Pasyanos et al.*, 1996] defined as follows:

$$\mathrm{VR} = \left(1 - \frac{d - d_{\mathrm{syn}}}{d}\right) \times 100 \tag{1}$$

$$\mathrm{RES/Pdc} = \frac{d - d_{\mathrm{syn}}}{d \times \mathrm{Pdc}}, \tag{2}$$

where Pdc is the percentage of DC during moment tensor decomposition, d is the observed waveform, and d_{syn} is the synthetic data summed over three components of all stations. The uncertainty of the best fit moment tensor is evaluated from bootstrap resampling tests [*Efron and Tibshirani*, 1991]. During these tests, we randomly select 14 out of 19 stations/bandwidths and determine the full moment tensor. This experiment is repeated 200 times to obtain statistically significant distributions for all elements of the moment tensor as well as the strike, slip, and rake angles. The standard deviations of these distributions are effective measures of variation.

In addition, we determine ground motion amplitudes using pseudo-acceleration (PSA) spectral amplitudes. Distances up to 400 km are selected to show the effect of attenuation, and a regional model [*Yenier and Atkinson*, 2015; *Atkinson et al.*, 2014] is used to obtain the moment magnitude and estimate the Brune-model [*Brune*, 1970] stress drop.

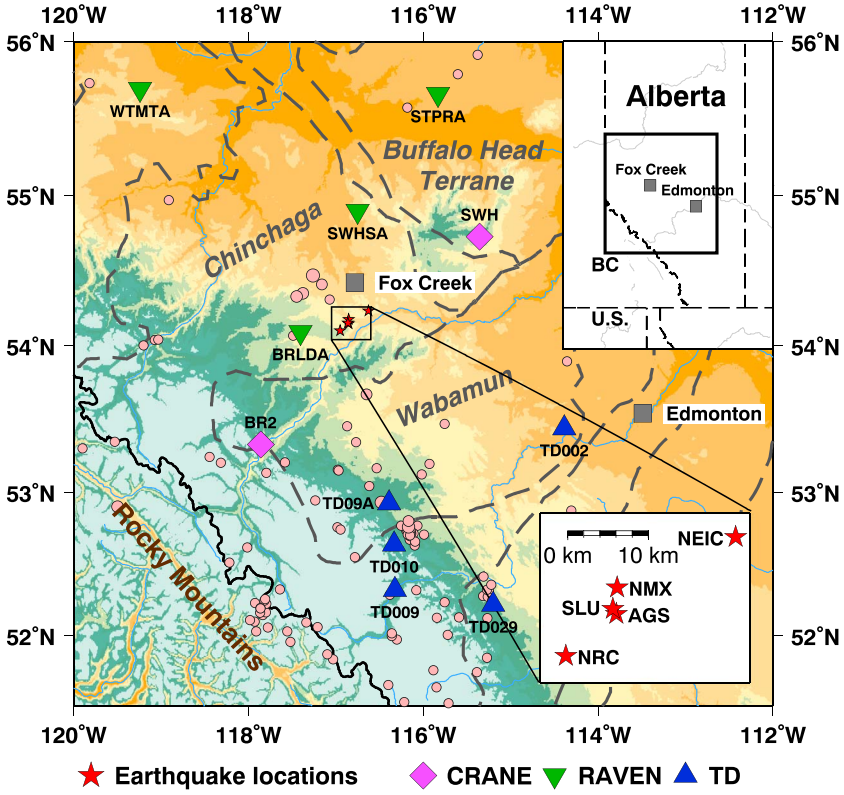

Figure 1. Spatial distributions of seismic stations (triangles and diamonds) and earthquakes recorded after 2006 (circles) with magnitudes greater than 3.0. The earthquake data are obtained from Alberta Geological Survey (2006–2010) [*Stern et al.*, 2013] and Natural Resources Canada (2011–2015, from http://earthquakescanada.nrcan.gc.ca/recent/index-eng.php, last accessed August 2015). The grey dashed lines denote the Proterozoic domain boundaries [*Clowes et al.*, 2002; *Ross et al.*, 1999]. The map inset in the lower right corner highlights the hypocenter locations reported by different agencies: Natural Resources Canada (NRC), Nanometrics Athena (NMX), Saint Louis University Earthquake Center (SLU), Alberta Geological Survey (AGS), and National Earthquake Information Center (NEIC).

3. Results

The focal mechanism, moment magnitude, source location, and depth are obtained as the best fit solution from high-frequency body waves recorded by 8 stations and low-frequency surface waves recorded by 11 stations. The final inversion result indicates an epicenter close to the reported source location by AGS (hereinafter referred to as AGS location), with an optimal depth of 3–4 km and a moment magnitude (**M**) of 3.9.

3.1. Focal Mechanism and Moment Tensor Decomposition

The solutions from waveform inversions generally achieved VRs greater than 70% regardless of whether one considers full, deviatoric, or pure DC moment tensor solutions. The fault plane solutions from these three different approaches are highly consistent, suggesting a strike-slip mechanism with candidate fault planes along E-W and N-S orientations (Figure 2). The components of the moment tensors and VRs are influenced by the modeling approach and data selection (see Table S1 in the supporting information). The results of full and deviatoric moment tensor inversions achieve identical VRs in all frequency ranges, indicating a negligible isotropic (for short, ISO) component (<4%) and a limited compensated-linear-vector-dipole (CLVD) component (see Figure 2). In comparison, the pure DC solutions determined through a forward routine yield lower VRs, especially at frequencies above 0.08 Hz. These VR values are comparable to those attained by SLU (<65%) based on inversions for pure DC sources. The dominance of the DC component makes RES/Pdc a reasonable metric for the assessment of hypocenter location and depth accuracies [*Ichinose et al.*, 1998].

It is worth noting that inversions based on low frequencies (VR ~90%) are more stable than their high-frequency counterpart (VR ~75%). On the other hand, the inclusion of higher frequencies imposes greater constraints on the direct *P* and *S* phases with relatively high signal-to-noise ratios and reduced

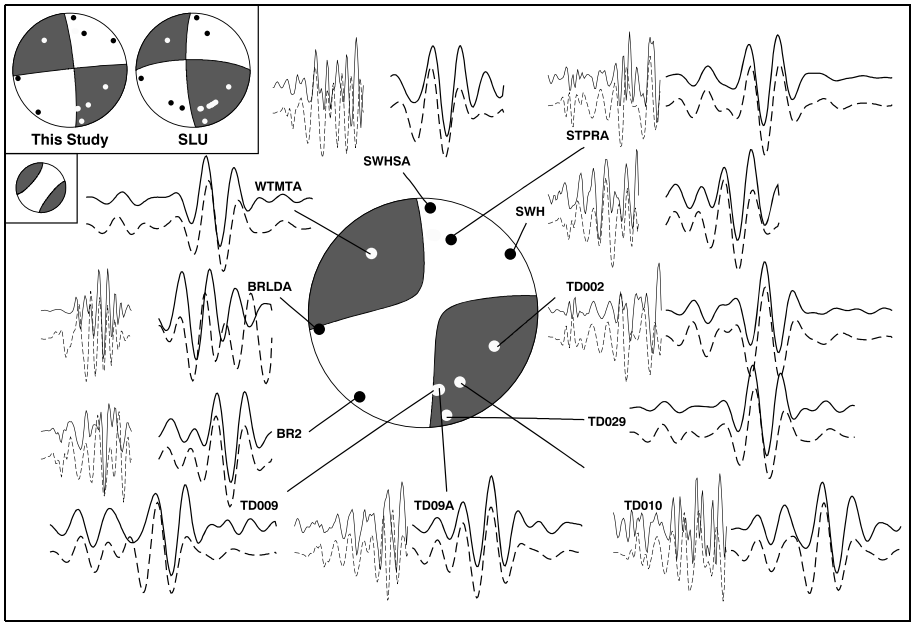

Figure 2. Inversion results and the vertical-component waveforms of low (0.05–0.1 Hz, 11 stations) and high (0.08–0.4 Hz, 8 stations) frequencies. The solid and dashed lines show the observed and best fitting synthetic data, respectively. The result of our full moment tensor inversion is shown in the center of the page and two DC solutions from forward modeling (left, this study) and moment tensor inversion (right, SLU, from http://www.eas.slu.edu/eqc/eqc_mt/MECH.NA/20150613235753/index.html, last accessed September 2015) are shown in the top left corner. The latter two moment tensors used slightly different data sets and hypocenter locations (see text for details). For a comparison, the non-DC component from the full moment tensor inversion is plotted beneath the DC solutions. In all cases, the shaded quadrants are compressive. The small circles on the focal mechanisms indicate compressional (open) and dilatational (solid) *P* wave first motion, determined from vertical component waveforms in the frequency range of 0.5–5.0 Hz. The takeoff angles are calculated from IASP91 [*Kennett and Engdahl*, 1991].

sensitivities to the complex subsurface velocities. The joint inversion procedure (our method of choice), which incorporates both high and low frequencies, represents a reasonable compromise between VR and Pdc.

3.2. Improving Hypocenter Location and Depth

The availability of nearby stations, especially two recently installed stations BR2 and SWH, enables us to provide a more accurate hypocenter location than was previously possible. To determine the best location and minimize its bias, we introduce 14 test locations within a grid of 20 km × 20 km as the input for a series of full moment tensor inversions of both body and surface waves (Figures 3a and 3b). This grid contains four out of five reported epicenter locations, centering on the AGS/SLU location. The VR and RES/Pdc values from all test locations of the epicenter are subsequently interpolated using 2-D spline algorithm [*Smith and Wessel*, 1990]. The highest observed VR is 69.1%, which is below the value of the final solution due to an assumed focal depth of 5 km, and the lowest RES/Pdc is ~7.4. The optimal location based on (1) high VR and (2) low RES/Pdc (see Figures 3a and 3b) is within 0.5 km of the center of test grid, coinciding with the proposed earthquake epicenter location (latitude 54.1742, longitude −116.8525) by AGS. Also notable is the low RES/Pdc toward the SSW (see Figure 3b), which reflects increased Pdc (e.g., 89% at NRC location; 81% at most south location) and reduced resolution along this orientation.

The optimal depth determined from independent inversions of low- and high-frequency ranges are 4.0 km and 3.1 km, respectively (Figure 3c). Both solutions exhibit relatively constant values between the depths of 2.5 and 4.5 km, beyond which the VR decreases substantially. The results of joint inversions are moderately dependent on the subjective weights (see Figure 3c) of the subsets of the data. An independent experiment based on inversions of the broadband (0.02–1.0 Hz) data yields a focal depth of 3.8 km (SLU), which also falls within our end-member models of 3–4 km.

3.3. Uncertainties

The reported hypocenter locations vary by as much as 26 km between the NRC and NEIC solutions. The variability of these solutions can be as large as 5 km [*Schultz et al.*, 2015b; *Farahbod et al.*, 2015] and is largely

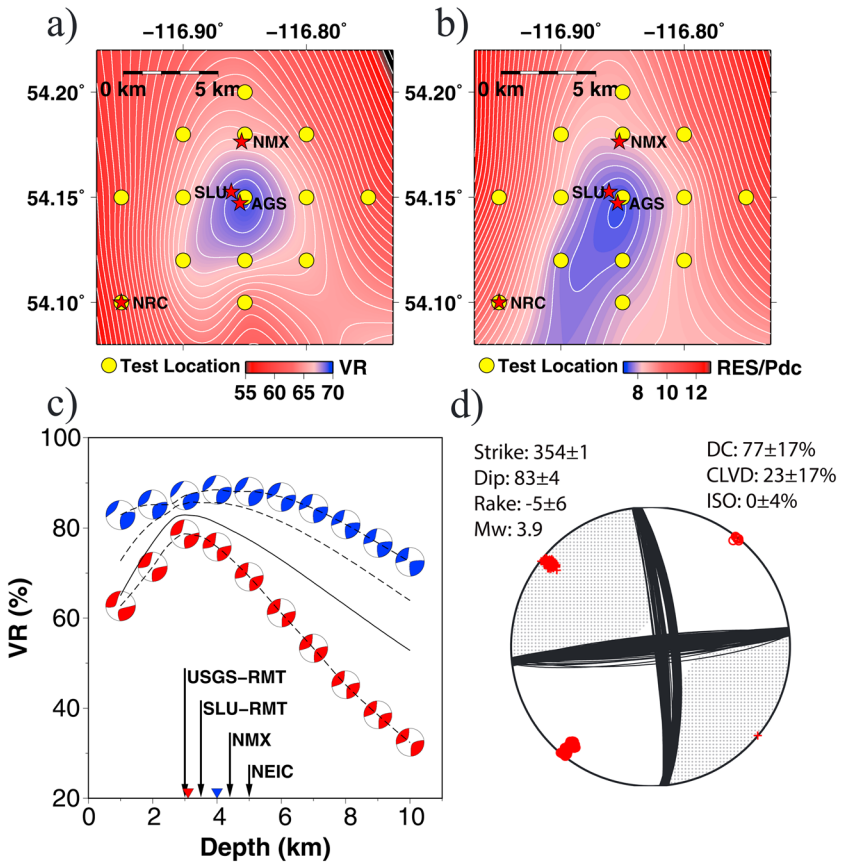

Figure 3. (a) Interpolated VR values (see equation (1)) for 14 uniformly distributed, hypothetical source locations (yellow circles). The stars indicate the four reported epicenters as denoted. The maximum VR is obtained near the center of the grid. (b) Interpolated RES/Pdc values (normalized residual, see equation (2)) for the same 14 source locations. The minimum RES/Pdc values roughly coincide with the AGS location and consistently low values are observed along a N-W orientation. (c) VR for a range of depths. The focal mechanism from independent inversions using body (red) and surface (blue) waves suggest optimal depths of 3 km (red triangle) and 4 km (blue triangle), respectively. The solid and dashed lines without focal mechanisms indicate the outcomes of joint inversions of surface and body waves with assumed amplitude ratios of 1 and 2. The arrows indicate the reported earthquake depths from four agencies. (d) Fault plane solutions determined from a bootstrap resampling test using 200 trials [*Efron and Tibshirani*, 1991] (see section 3.3 for details).

attributable to the availability/choice of stations and picking errors of the arrival times. Based on improved station coverage and a grid search algorithm (see section 3.2), we are able to determine the epicenter location and depth to an accuracy of ~1 km. The orientations of two candidate fault plane solutions and stress regimes remain stable (see Figure 3d). The strike, dip, and rake values determined from the means of their distributions equal to 354°, 83°, and −5°, respectively. The largest variation is only 6° (in rake value). To quantify the uncertainties associated with velocity inaccuracy, we introduce a 20% reduction to the input model at all crustal depths. The inverted fault angles (strike, dip, and rake) only differ by an average of 10° from those of the unperturbed structure (see Figure S1 in the supporting information). However, the bootstrapping test shows a standard error of 17% in CLVD based on the 95% confidence interval, which is comparable to the observed CLVD contribution (23%) to the final focal solution. Hence, we conclude that the CLVD component is poorly constrained and most likely represents only a modest contribution to the focal mechanism.

3.4. Analysis of Ground Motion Amplitudes

Large variability also exists in reported observatory magnitude measures of Richter magnitude (M_L 4.6; NEIC) and body wave amplitude (mb_Lg 4.0; SLU) [*Nuttli*, 1973; *Herrmann and Nutti*, 1982]. For this reason, we use the vertical-component 1 Hz PSA amplitudes (with 5% damping) of publicly available stations, and a distance less than 400 km, to provide an alternative estimate of moment magnitude (see the algorithm [*Atkinson et al.*, 2014]). Using the model for central and eastern North America (CENA), which provides the best fit to

the observed attenuation, we obtain a value (**M** = 3.9, see Figure S2a) identical to that from our moment tensor inversion. We further estimate the source spectrum for the event by correcting all amplitudes to the source, following the equations provided in *Yenier and Atkinson* [2015]. After correcting for average site effects [*Farrugia et al.*, 2015], we obtained a stress drop of 6 MPa by matching the high-frequency amplitudes of the median horizontal PSA amplitudes (the observed earthquake source function, see *Yenier and Atkinson* [2015]). The value of 6 MPa is near the upper range of the stress drops for shallow (induced) events in CENA, consistent with those determined for regional events in other studies [*Atkinson et al.*, 2014; *Rebollar et al.*, 1982].

4. Discussion

The earthquake source parameters from our moment tensor inversions offer improved constraints on the hypocenter location, faulting geometry, and the state of stress in the subsurface, which are all critical in the assessment of seismic hazard in central Alberta. The final focal mechanism solution produced outstanding fit to the recorded three-component waveforms, reaching a VR as high as 79.8% (see Figure 2). The inverted magnitude of this event (**M** = 3.93) is consistent with the solution obtained using PSA amplitudes and an independent, pure DC moment tensor inversion (**M** = 3.94; SLU). This value, which falls slightly below the red light threshold (**M** = 4.0) defined by the provincial traffic light regulation [*Alberta Energy Regulator*, 2015], is significantly smaller than the initial report of $M_L = 4.4$.

Aside from a relatively large magnitude, this event attracted significant media attention due to its proximity to the unconventional oil and gas exploration. The earthquake is located at ~27 km south of Fox Creek within the Duvernay shale gas play, an area characterized by significant HF activities (e.g., Kaybob south and Pine Creek reservoirs). Multistage fracturing is conducted [*Haug et al.*, 2013] with horizontal wells drilled to depths up to 3.5 km, (Figure 4), close to the basement (~4 km) [*Pilkington et al.*, 2000; *Bachu*, 1993; *Majorowicz et al.*, 2014]. Five horizontal wells have been identified within 2 km of our proposed hypocenter location. Based on recently published reports (obtained through *GeoSCOUT*), HF operations took place during the month preceding the earthquake. The publicly accessible records suggest no evidence of other major industrial activities associated with enhanced oil recovery or waste water disposal in the vicinity during 2015. The depth of the earthquake determined from our full moment tensor inversion is 3–4 km, overlapping with the dolostone-hosted shale gas reservoirs in the depth range of 3.1–3.6 km [*Rokosh et al.*, 2012] and the bottom depth of HF. In WCSB, correlations between the focal and injection depths have been documented in the Cordel Field [*Schultz et al.*, 2014], Cardston [*Schultz et al.*, 2015c], Crooked Lake [*Schultz et al.*, 2015a], Rocky Mountain House [*Rebollar et al.*, 1982], and British Columbia [*BC Oil and Gas Commission*, 2012, 2014], where earthquake swarms with magnitudes 1–3.5 are possibly caused by increased pore pressure near the basement. Recently, larger earthquakes triggered by fluid injection/extraction have been observed in Colorado [*McGarr*, 2014; *Ake et al.*, 2005], Ohio [*Skoumal et al.*, 2015; *Friberg et al.*, 2014; *Kim*, 2013], and Switzerland [*Evans et al.*, 2012; *Häring et al.*, 2008]. Judging from the hypocenter location, focal depth, and timing, an association of this event with nearby HF operations cannot be excluded.

Among the induced earthquakes observed worldwide, a moderate percentage shows a strike-slip focal mechanism [*Zang et al.*, 2014]. Movements along buried faults, which are difficult to detect based on active-source seismic surveys, are likely responsible [*McNamara et al.*, 2015; *Zhang et al.*, 2013]. Our moment tensor inversions with full, deviatoric, and pure DC constraints suggest ~80% DC and a strike-slip mechanism with vertical fault planes. The stability of the fault geometry is further evidenced by the consistency between our best fit result and the solution from SLU, determined from independent crustal velocity and attenuation models (see Figure 2). The two candidate fault planes, which are E-W and N-S oriented, suggest a NE-SW maximum compressional axis consistent with the regional crustal stress orientations from borehole breakouts and drilling-induced fractures [*Reiter et al.*, 2014; *Heidbach et al.*, 2010] (see Figure 4). Similar compressional axes are also obtained from other **M** > 3.5 earthquakes in central and western Alberta [*Eaton and Mahani*, 2015; *Kao et al.*, 2012]. However, the mechanism of this earthquake (strike slip) differs considerably from those of the aforementioned regional events (mainly normal and thrust) and favors a potential association with a preexisting vertical fault.

Based on geochemical, well logging, and reflection seismic data, *Green and Mountjoy* [2005] suggest that high-angle faults are present 10 km away from our proposed hypocenter location (see Figure 4). At a depth of 3.1–3.8 km, two of these faults mark the boundaries of a 100 m wide graben with a dimension of ~0.7 km [*Green and Mountjoy*, 2005]. The expected maximum earthquake magnitude on a fault of such dimension

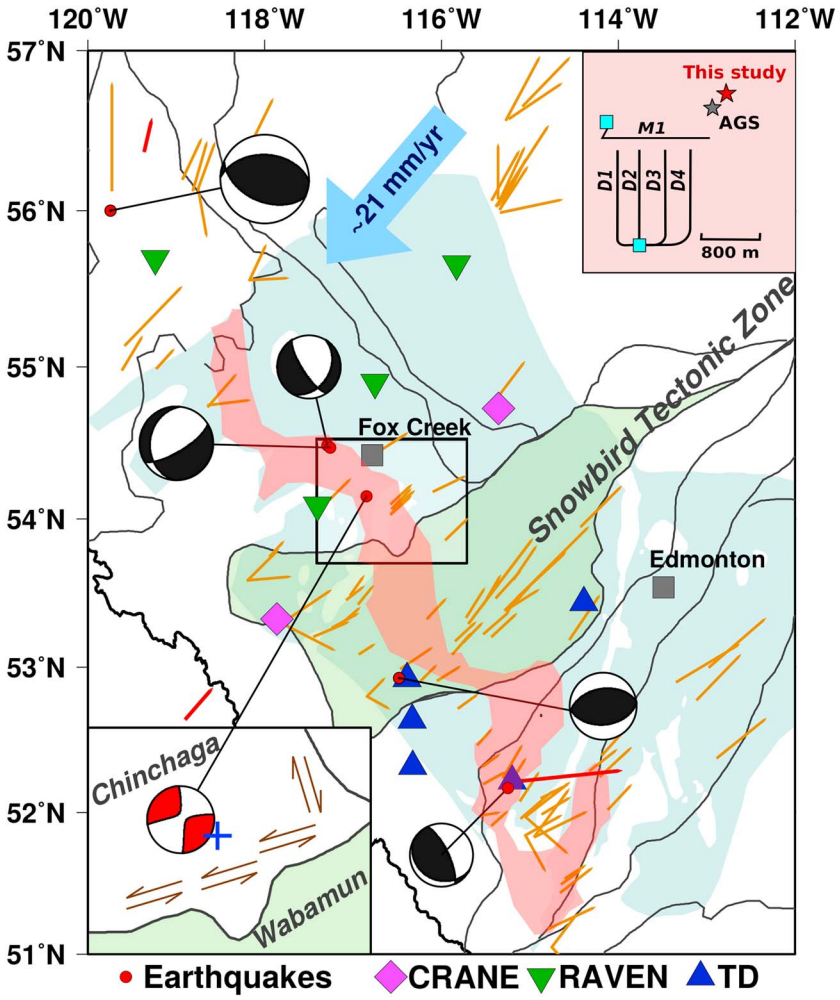

Figure 4. Crustal stress and available focal mechanisms of **M** > 3.5 earthquakes superimposed on a tectonic map of our study region. The thin solid lines denote the proposed Proterozoic domain boundaries [*Ross et al.*, 1999]. The rate and direction of the present-day plate motion are indicated by the blue arrow. The crustal stress from borehole breakout data are represented in yellow, and those determined from seismic source solutions are shown in red [*Heidbach et al.*, 2010]. The bottom left map inset highlights the source region, and the interpreted fault movements are indicated by the double arrows. The blue cross marks a graben (faults) in the depth range of 3.1–3.8 km, mapped by an earlier active-source seismic survey [*Green and Mountjoy*, 2005]. The area shaded in green denotes the Wabamun domain. The area shaded in light blue indicates the shape and location of the Duvernay Formation and the rich-gas region is highlighted in red (obtained from *Oilweek Magazine* [2013]). The map inset in the top right corner shows the hypocenter locations (stars) relative to two HF wells (blue squares) that were active during June 2015. The bottom depths and the latest well completion dates are as follows: M1: 2415.0 m, 7 June 2015; D1: 3434.7 m, 2 June 2015; D2: 3433.9 m, 5 June 2015; D3: 3445.0 m, 10 May 2015; D4: 3446.1 m, 11 May 2015.

is close to 4 [*Zang et al.*, 2014; *Wells and Coppersmith*, 1994], comparable to that of the 13 June earthquake. While these faults may not be directly associated with this event, reactivation of a similar vertical fault with a common origin is a realistic possibility.

Proterozoic tectonic history of the study region is also conducive to significant crustal deformation and the existence of buried faults. In the proximity of the epicenter location to the Snowbird Tectonic Zone (STZ), a transcontinental suture [*Hoffman*, 1988; *Ross et al.*, 2000; *Berman et al.*, 2007] or shear zone [*Lewry et al.*, 1994; *Hanmer et al.*, 1995] that bifurcates around the Proterozoic Wabamun domain (see Figure 4). The southern branch of STZ has been widely linked to subduction, while the origin of the northern branch (~30 km away from the proposed earthquake hypocenter location) remains debated. Regardless of the nature of STZ, the interaction/collision between the Proterozoic microcontinents (Wabamun and Chinchaga

domains, see Figure 1) is potentially responsible for preexisting faults parallel, or perpendicular, to the domain boundary.

It is worth noting that despite being strike slip, the 13 June earthquake may contain ~20% non-DC components. The interpretation of CLVD remains controversial, mainly centering on (1) an improper assumption that multiple subevents [*Kuge and Kawakatsu*, 1990] or fracturing along on curve/complex geometry [*Kawakatsu*, 1991] can be represented by a single source and (2) fluid-driven opening (or closing) of tensile cracks [*Miller et al.*, 1998]. The second explanation is favored by shallow earthquakes, especially at depth involving fluid injection or extraction [*Frohlich*, 1994; H. Zhang et al., Discriminating induced seismicity from natural earthquakes using moment tensors and source spectra, submitted to *Journal of Geophysics Research Solid Earth*, 2015]. The horizontal CLVD obtained by this study (see Figure 2) are frequently observed in microearthquakes in connection with HF [*Baig and Urbancic*, 2010]. Whether the same type of mechanism is responsible for earthquakes that are orders of magnitude larger, such as this case, remains questionable.

5. Conclusions

This study presents an updated solution of seismic source parameters for a moderate earthquake near Fox Creek, Alberta, using time domain full moment tensor inversions. We conclude the following:

1. The location of this event is 27 km south of the town of Fox Creek and the focal depth is between 3 and 4 km, at the junction between sedimentary and basement layers.
2. The magnitude of this event determined from full moment tensor inversions is **M** = 3.9, consistent with that from PSA calculations; the observed ground motions suggest a stress drop of 6 MPa.
3. The focal mechanism is predominately vertical strike slip with N-S and E-W oriented fault planes. The maximum stress direction is compatible with the contemporaneous crustal state of stress.
4. We observed 23% non-DC component, which is dominated by a horizontal CLVD with a relatively large uncertainty.

A reliable correlation or dissociation between this earthquake and local shale gas exploration activities will require improved subsurface information and full access to the well completion data. The key parameters of this event (e.g., timing, depth, and mechanism) are symptomatic of an earthquake induced by HF operations in the vicinity of Fox Creek, Alberta. Overall, the broadband seismic data and, the approach adopted by this study, may benefit a future assessment of the seismic hazard in and around the WCSB.

Acknowledgments

We thank NRC, NMX, SLU, NEIC, and AGS for preliminary information of this earthquake and Honn Kao for comments on the hypocenter locations. Data of RAVEN and TD stations are requested from Incorporated Research Institutions for Seismology (IRIS); the TD stations are contributed to IRIS by TransAlta. We thank Yunfeng Chen and Ramin Dokht for scientific and programming help. The authors are grateful to Cliff Frohlich and Art McGarr for their insightful reviews. Moment tensors were computed using the tdmt-invc-iso package developed by Douglas Dreger and Sean Ford of the Berkeley Seismological Laboratory, and Green's functions were computed using the FKRPROG software developed by Chandan Saikia. We acknowledge research funding from the Natural Sciences and Engineering Research Council of Canada and Helmholtz-Alberta Initiative.

References

Ake, J., K. Mahrer, D. O'Connell, and L. Block (2005), Deep-injection and closely monitored induced seismicity at Paradox Valley, Colorado, *Bull. Seismol. Soc. Am.*, *95*(2), 664–683, doi:10.1785/0120040072.

Alberta Energy Regulator (2015), Subsurface order 2. [Available at https://aer.ca/documents/orders/subsurface-orders/SO2.pdf.]

Atkinson, G. M., D. W. Greig, and E. Yenier (2014), Estimation of moment magnitude (*M*) for small events (*M* < 4) on local networks, *Seismol. Res. Lett.*, *85*(5), 1116–1124, doi:10.1785/0220130180.

Bachu, S. (1993), Basement heat flow in the Western Canada sedimentary basin, *Tectonophysics*, *222*(1), 119–133, doi:10.1016/0040-1951(93)90194-O.

Baig, A., and T. Urbancic (2010), Microseismic moment tensors: A path to understanding frac growth, *Leading Edge*, *29*(3), 320–324.

BC Oil and Gas Commission (2012), Investigation of observed seismicity in the Horn River Basin. [Available at http:// www.bcogc.ca/sites/default/files/documentation/technical-reports/investigation-observed-seismicity-montney-trend.pdf.]

BC Oil and Gas Commission (2014), Investigation of observed seismicity in the Montney Trend. [Available at http://www.bcogc.ca/document.aspx?documentID=1270], (December), 32.

Bent, A. L. (2011), Moment magnitude (M_W) conversion relations for use in hazard assessment in eastern Canada, *Seismol. Res. Lett.*, *82*(6), 984–990.

Berman, R., W. Davis, and S. Pehrsson (2007), Collisional Snowbird tectonic zone resurrected: Growth of Laurentia during the 1.9 accretionary phase of the Hudsonian orogeny, *Geology*, *35*(10), 911–914, doi:10.1130/G23771A.1.

Brune, J. N. (1970), Tectonic stress and the spectra of seismic shear waves from earthquakes, *J. Geophys. Res.*, *75*(26), 4997–5009.

Chen, W., S. Ni, H. Kanamori, S. Wei, Z. Jia, and L. Zhu (2015a), CAPjoint, a computer software package for joint inversion of moderate earthquake source parameters with local and teleseismic waveforms, *Seismol. Res. Lett.*, *86*(2A), 432–441, doi:10.1785/0220140167.

Chen, Y., Y. J. Gu, R. M. Dokht, and M. D. Sacchi (2015b), Crustal imprints of Precambrian orogenesis in western Laurentia, *J. Geophys. Res. Solid Earth*, *120*, 5051–5069, doi:10.10002/2014JB011802.

Clowes, R. M., M. J. Burianyk, A. R. Gorman, and E. R. Kanasewich (2002), Crustal velocity structure from SAREX, the Southern Alberta Refraction Experiment, *Can. J. Earth Sci.*, *39*(3), 351–373, doi:10.1139/e01-070.

Dreger, D. S. (2003), 85.11 TDMT_INV: Time domain seismic moment tensor inversion, *Int. Handb. Earthquake Eng. Seismolog.*, *81b*, 1627.

Eaton, D. W., and A. B. Mahani (2015), Focal mechanisms of some inferred induced earthquakes in Alberta, Canada, *Seismol. Res. Lett.*, *86*(4), 1–8, doi:10.1785/0220150066.

Efron, B., and R. Tibshirani (1991), Statistical data analysis in the computer age, *Science*, *253*(5018), 390–395.

Evans, K. F., A. Zappone, T. Kraft, N. Deichmann, and F. Moia (2012), A survey of the induced seismic responses to fluid injection in geothermal and CO_2 reservoirs in Europe, *Geothermics*, *41*, 30–54, doi:10.1016/j.geothermics.2011.08.002.

Farahbod, A. M., H. Kao, D. M. Walker, and J. F. Cassidy (2015), Investigation of regional seismicity before and after hydraulic fracturing in the Horn River Basin, northeast British Columbia, *Can. J. Earth Sci.*, *52*(2), 112–122, doi:10.1139/cjes-2014-0162.

Farrugia, D., E. Paolucci, S. D'Amico, and P. Galea (2015), Inversion of surface wave data for shear wave velocity profiles: Case studies of thick buried low-velocity layers in Malta, Geophysical Research Abstracts Vol. 17, EGU2015-448 presented at 2015 EGU General Assembly, Vienna, Austria, 12–17 Apr.

Friberg, P. A., G. M. Besana-Ostman, and I. Dricker (2014), Characterization of an earthquake sequence triggered by hydraulic fracturing in Harrison County, Ohio, *Seismol. Res. Lett.*, *85*(6), 1295–1307, doi:10.1785/0220140127.

Frohlich, C. (1994), Earthquakes with non-double-couple mechanisms, *Science*, *264*(5160), 804–809.

Green, D. G., and E. W. Mountjoy (2005), Fault and conduit controlled burial dolomitization of the Devonian west-central Alberta Deep Basin, *Bull. Can. Pet. Geol.*, *53*(2), 101–129, doi:10.2113/53.2.101.

Gu, Y. J., and L. Shen (2015), Noise correlation tomography of Southwest Western Canada Sedimentary Basin, *Geophys. J. Int.*, *202*(1), 142–162, doi:10.1093/gji/ggv100.

Gu, Y. J., A. Okeler, L. Shen, and S. Contenti (2011), The Canadian Rockies and Alberta Network (CRANE): New constraints on the Rockies and Western Canada Sedimentary Basin, *Seismol. Res. Lett.*, *82*(4), 575–588, doi:10.1785/gssrl.82.4.575.

Hanmer, S., M. Williams, and C. Kopf (1995), Striding-Athabasca mylonite zone: Implications for the Archean and Early Proterozoic tectonics of the western Canadian Shield, *Can. J. Earth Sci.*, *32*(2), 178–196.

Häring, M. O., U. Schanz, F. Ladner, and B. C. Dyer (2008), Characterisation of the Basel 1 enhanced geothermal system, *Geothermics*, *37*(5), 469–495, doi:10.1016/j.geothermics.2008.06.002.

Haug, K. M., J. M. Dongas, and J. Warren (2013), A review of the potential correlation between low-magnitude earthquakes and oil and gas industry activity in Alberta, *Alberta Energy Regulator, AER/AGS Open File Report, 2013-16*, 43 p.

Heidbach, O., M. Tingay, A. Barth, J. Reinecker, D. Kurfeß, and B. Müller (2010), Global crustal stress pattern based on the World Stress Map database release 2008, *Tectonophysics*, *482*(1–4), 3–15, doi:10.1016/j.tecto.2009.07.023.

Henry, C., J. Woodhouse, and S. Das (2002), Stability of earthquake moment tensor inversions: Effect of the double-couple constraint, *Tectonophysics*, *356*(1), 115–124, doi:10.1016/S0040-1951(02)00379-7.

Herrmann, R. B., and O. W. Nuttli (1982), Magnitude: The relation of M_L to m_{bLg}, *Bull. Seismol. Soc. Am.*, *72*(2), 389–397.

Hoffman, P. F. (1988), United plates of America, the birth of a craton-Early Proterozoic assembly and growth of Laurentia, *Annu. Rev. Earth Planet. Sci.*, *16*, 543–603.

Ichinose, G. A., K. D. Smith, and J. G. Anderson (1998), Moment tensor solutions of the 1994 to 1996 double spring flat, Nevada, earthquake sequence and implications for local tectonic models, *Bull. Seismol. Soc. Am.*, *88*(6), 1363–1378.

Jones, A. G. (2002), Magnetotelluric and teleseismic study across the Snowbird Tectonic Zone, Canadian Shield: A Neoarchean mantle suture?, *Geophys. Res. Lett.*, *29*(17), 1829, doi:10.1029/2002GL015359.

Julian, B. R., A. D. Miller, and G. Foulger (1998), Non-double-couple earthquakes 1. Theory, *Rev. Geophys.*, *36*(4), 525–549.

Kawakatsu, H. (1991), Enigma of earthquakes at ridge-transform-fault plate boundaries distribution of non-double couple parameter of Harvard CMT solutions, *Geophys. Res. Lett.*, *18*(6), 1103–1106.

Kennett, B., and E. Engdahl (1991), Travel times for global earthquake location and phase identification, *Geophys. J. Int.*, *105*(2), 429–465.

Kim, W.-Y. (2013), Induced seismicity associated with fluid injection into a deep well in Youngstown, Ohio, *J. Geophys. Res. Solid Earth*, *118*, 3506–3518, doi:10.1002/jgrb.50247.

Kuge, K., and H. Kawakatsu (1990), Analysis of a deep "non-double-couple" earthquake using very broadband data, *Geophys. Res. Lett.*, *17*(3), 227–230.

Lewry, J., Z. Hajnal, A. Green, S. Lucas, D. White, M. Stauffer, K. Ashton, W. Weber, and R. Clowes (1994), Structure of a Paleoproterozoic continent-continent collision zone: A LITHOPROBE seismic reflection profile across the Trans-Hudson Orogen, Canada, *Tectonophysics*, *232*(1), 143–160.

Majorowicz, J., et al. (2014), The first deep heat flow determination in crystalline basement rocks beneath the Western Canadian Sedimentary Basin, *Geophys. J. Int.*, *197*(2), 731–747, doi:10.1093/gji/ggu065.

McGarr, A. (2014), Maximum magnitude earthquakes induced by fluid injection, *J. Geophys. Res. Solid Earth*, *119*, 1008–1019, doi:10.1002/2013JB010597.

McNamara, D., et al. (2015), Efforts to monitor and characterize the recent increasing seismicity in central Oklahoma, *Leading Edge*, *34*(6), 628–639, doi:10.1190/tle34060628.1.

Miller, A., G. Foulger, and B. Julian (1998), Non-double-couple earthquakes 2. Observations, *Rev. Geophys.*, *36*(4), 551–568.

Minson, S. E., and D. S. Dreger (2008), Stable inversions for complete moment tensors, *Geophys. J. Int.*, *174*(2), 585–592, doi:10.1111/j.1365-246X.2008.03797.x.

Nuttli, O. W. (1973), Seismic wave attenuation and magnitude relations for eastern North America, *J. Geophys. Res.*, *78*(5), 876–885.

Oilweek Magazine (2013), Delving into the Duvernay. [Available at http://oilweek1.rssing.com/browser.php?indx=10975088&item=82.]

Pasyanos, M. E., D. S. Dreger, and B. Romanowicz (1996), Toward real-time estimation of regional moment tensors, *Bull. Seismol. Soc. Am.*, *86*(5), 1255–1269.

Pilkington, M., W. F. Miles, G. M. Ross, and W. R. Roest (2000), Potential-field signatures of buried Precambrian basement in the Western Canada Sedimentary Basin, *Can. J. Earth Sci.*, *37*(11), 1453–1471, doi:10.1139/e00-020.

Rebollar, C., E. Kanasewich, and E. Nyland (1982), Source parameters from shallow events in the Rocky Mountain House earthquake swarm, *Can. J. Earth Sci.*, *19*(5), 907–918.

Reiter, K., O. Heidbach, D. Schmitt, K. Haug, M. Ziegler, and I. Moeck (2014), A revised crustal stress orientation database for Canada, *Tectonophysics*, *636*, 111–124, doi:10.1016/j.tecto.2014.08.006.

Rokosh, C. D., S. D. Anderson, A. P. Beaton, M. Berhane, and J. Pawlowicz (2010), Geochemical and geological characterization of the Duvernay and Muskwa Formation in Alberta, paper presented at Canadian Unconventional Resources and International Petroleum Conference, Calgary, Alberta, Canada, 19–21 Oct., Soc. of Petrol. Eng., doi:10.2118/137799-MS.

Rokosh, C. D., S. Lyster, S. D. A. Anderson, A. P. Beaton, H. Berhane, T. Brazzoni, D. Chen, Y. Cheng, and J. G. Pawlowicz (2012), Summary of Alberta's shale- and siltstone-hosted hydrocarbon resource potential, *Energy Resources Conservation Board, ERCB/AGS Open File Report 2012-06*, 327 p.

Ross, A., G. R. Foulger, and B. R. Julian (1999), Source processes of industrially-induced earthquakes at the Geysers geothermal area, California, *Geophysics*, *64*(6), 1877–1889, doi:10.1190/1.1444694.

Ross, G. M., D. W. Eaton, D. E. Boerner, and W. Miles (2000), Tectonic entrapment and its role in the evolution of continental lithosphere: An example from the Precambrian of western Canada, *Tectonics*, *19*(1), 116–134.

Saikia, C. K. (1994), Modified frequency-wavenumber algorithm for regional seismograms using Filon's quadrature: Modelling of L_g waves in eastern North America, *Geophys. J. Int.*, *118*(1), 142–158.

Schultz, R., and V. Stern (2015), The Regional Alberta Observatory for Earthquake Studies Network (RAVEN), CSEG Recorder.

Schultz, R., V. Stern, and Y. J. Gu (2014), An investigation of seismicity clustered near the Cordel Field, west central Alberta, and its relation to a nearby disposal well, *J. Geophys. Res. Solid Earth*, *119*, 3410–3423, doi:10.1002/2013JB010836.

Schultz, R., V. Stern, M. Novakovic, G. Atkinson, and Y. J. Gu (2015a), Hydraulic fracturing and the Crooked Lake sequences: Insights gleaned from regional seismic networks, *Geophys. Res. Lett.*, *42*, 2750–2758, doi:10.1002/2015GL063455.

Schultz, R., V. Stern, Y. J. Gu, and D. Eaton (2015b), Detection threshold and location resolution of the Alberta Geological Survey earthquake catalogue, *Seismol. Res. Lett.*, *86*(2A), 385–397, doi:10.1785/0220140203.

Schultz, R., S. Mei, D. Pană, V. Stern, Y. J. Gu, A. Kim, and D. Eaton (2015c), The Cardston earthquake swarm and hydraulic fracturing of the Exshaw Formation (Alberta Bakken play), *Bull. Seismol. Soc. Am.*, *105*(6), 2871–2884, doi:10.1785/0120150131.

Skoumal, R. J., M. R. Brudzinski, and B. S. Currie (2015), Earthquakes induced by hydraulic fracturing in Poland Township, Ohio, *Bull. Seismol. Soc. Am.*, *105*(1), 189–197, doi:10.1785/0120140168.

Smith, W., and P. Wessel (1990), Gridding with continuous curvature splines in tension, *Geophysics*, *55*(3), 293–305.

Stern, V., R. Schultz, L. Shen, Y. Gu, and D. Eaton (2013), Alberta earthquake catalogue, version 1.0: September 2006 through December 2010, *AER/AGS Open File Rep. 2013-15*, vol. 15, 36 pp., Alberta Geol. Surv., Alberta, Canada. [Available at http://www.ags.gov.ab.ca/publications/ofr/PDF/ofr_2013_15.pdf.]

Switzer, S., W. Holland, D. Christie, G. Graf, A. Hedinger, R. McAuley, R. Wierzbicki, and J. Packard (1994), Devonian Woodbend-Winterburn strata of the Western Canada Sedimentary Basin, in *Geological Atlas of the Western Canada Sedimentary Basin*, edited by G. D. Mossop and I. Shetsen, pp. 165–202, Can. Soc. of Pet. Geol. and Alberta Res. Counc., Calgary, Can.

Welford, J. K., and R. M. Clowes (2006), Three-dimensional seismic reflection investigation of the upper crustal Winagami sill complex of northwestern Alberta, Canada, *Geophys. J. Int.*, *166*(1), 155–169, doi:10.1111/j.1365-246X.2006.02805.x.

Wells, D. L., and K. J. Coppersmith (1994), New empirical relationships among magnitude, rupture length, rupture width, rupture area, and surface displacement, *Bull. Seismol. Soc. Am.*, *84*(4), 974–1002.

Yenier, E., and G. M. Atkinson (2015), Regionally adjustable generic ground-motion prediction equation based on equivalent point-source simulations: Application to central and eastern North America, *Bull. Seismol. Soc. Am.*, *105*(4), 1989–2009, doi:10.1785/0120140332.

Zang, A., V. Oye, P. Jousset, N. Deichmann, R. Gritto, A. McGarr, E. Majer, and D. Bruhn (2014), Analysis of induced seismicity in geothermal reservoirs—An overview, *Geothermics*, *52*, 6–21, doi:10.1016/j.geothermics.2014.06.005.

Zelt, C., and R. Ellis (1990), Crust and upper mantle Q from seismic refraction data: Peace River region, *Can. J. Earth Sci.*, *27*(8), 1040–1047.

Zhang, Y., et al. (2013), Hydrogeologic controls on induced seismicity in crystalline basement rocks due to fluid injection into basal reservoirs, *Groundwater*, *51*(4), 525–538, doi:10.1111/gwat.12071.

Erratum

In the originally published version of this article, typographical errors were found in the legend of Figure 2. The following have since been corrected, and this version may be considered the authoritative version of record.

In the legend of Figure 2, "The small circles on the focal mechanisms indicate compressional (solid) and dilatational (open) *P* wave first motion," has been changed to "The small circles on the focal mechanisms indicate compressional (open) and dilatational (solid) *P* wave first motion,".